# Radio-Frequency Interference Estimation for Multiple Random Noise Sources

Ling Zhang, *Student Member, IEEE*, Haochen Yang, *Student Member, IEEE*, Xiangrui Su, *Student Member, IEEE*, Qiaolei Huang, Jagan Rajagopalan, Deepak Pai, Chulsoon Hwang, *Senior Member, IEEE*, and Jun Fan, *Fellow, IEEE*

***Abstract*—As more compact designs and more assembled function modules are utilized in modern electronic devices, radio-frequency interference (RFI) source reconstruction is becoming more challenging because different noise sources may contribute simultaneously. This article presents a novel methodology to reconstruct multiple random noise sources on a real-world product, including several double-data-rate (DDR) memory modules and a high-speed connector. The DDR modules located beneath a heatsink cause random noise-like signals, which renders phase measurements challenging. An approach based on the tuned-receiver mode of a vector network analyzer is developed to measure the field phase from the random DDR signals, which can be further modeled with a Huygens' box using the measured field magnitude and phase. Moreover, the connector can be modeled using an equivalent magnetic dipole. Furthermore, the total RFI power from the DDR memory modules and the high-speed connector, which generate uncorrelated RFI noise, is found to equal the summation of the individual power values obtained by an root mean square detector, which can be mathematically corroborated. Using the proposed method, the reconstructed source model can predict RFI values close to measurement results with less than 5 dB deviation.**

***Index Terms*—Double-data-rate (DDR), Huygens' box, magnetic dipole, multiple sources, radio-frequency interference (RFI), source reconstruction, uncorrelated sources.**

## I. Introduction

RADIO-FREQUENCY interference (RFI) is becoming increasingly important in modern wireless electronic devices, as their sizes become smaller and more function modules are densely assembled. RFI noise from different components, such as CPUs, memory modules, integrated circuits (ICs), heatsinks, and connectors, can simultaneously interfere with the receiving antenna and degrade receiver sensitivity [1]–[7], as illustrated in Fig. 1. The characterization of multiple RFI noise sources is necessary to better understand radiation physics and develop mitigation methods [8].

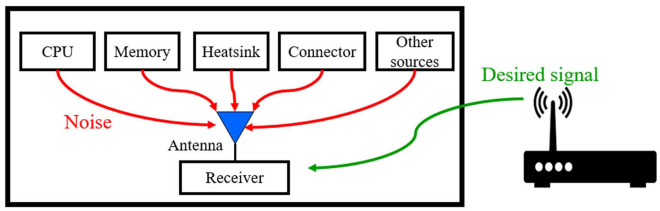


Fig. 1. Typical RFI problem: multiple RFI noise sources may coexist within a single electronic device.

There have been numerous studies on different methods for RFI source reconstruction. Dipole-moment arrays [1], [9]–[14] have been commonly used to model emissions and to estimate near-field coupling from ICs or printed circuit boards (PCBs). The near field is obtained on a plane above the sources, where both magnitude and phase are needed to calculate a dipole array. Huygens' box is another tool for reconstructing near-field sources [6], [7], [15]–[17]. Here, the tangential E or H fields on the Huygens' box surfaces are acquired, and again, both the magnitude and phase are needed. Simulations have been used to verify this Huygens' box methodology [15], [17], in which the magnitude and phase of the tangential fields are easy to simulate. In addition, some measurements have been performed to capture tangential fields, including the magnitude and phase on the Huygens' box [6], [16]. In [6], the vertical E field was measured along the gap between a heatsink and IC, while in [16], the tangential *H* field was measured on an imaginary Huygens' box above an IC source.

The dipole-moment and Huygens' box methods are effective for near-field source modeling if phase information is available. The studies mentioned above using these two methods [1], [6], [10], [12]–[14], [16] attained phase values from measurements. In some of these studies [6], [10], [12], a vector network analyzer (VNA) was used to excite a passive device, and the phase was obtained by measuring $S_{21}$. In the other works [1], [13], [14], [16], the phase was acquired by finding a stable measured signal or a signal synchronized to the measured signal as a phase

Manuscript received April 24, 2021; revised September 1, 2021; accepted September 29, 2021. This work was supported by the National Science Foundation under Grant IIP-1916535. *(Corresponding author: Jun Fan.)*

Ling Zhang is with the College of Information Science and Electronic Engineering, Zhejiang University, Hangzhou 310027, China, and also with the Electromagnetic Compatibility Laboratory, Missouri University of Science and Technology, Rolla, MO 65409 USA (e-mail: lingzhang_zju@zju.edu.cn).

Haochen Yang is with the College of Information Science and Electronic Engineering, Zhejiang University, Hangzhou 310027, China (e-mail: haochenyang@zju.edu.cn).

Xiangrui Su, Chulsoon Hwang, and Jun Fan are with the Electromagnetic Compatibility Laboratory, Missouri University of Science and Technology, Rolla, MO 65409 USA (e-mail: suxia@mst.edu; hwangc@mst.edu; jfan@mst.edu).

Qiaolei Huang, Jagan Rajagopalan, and Deepak Pai are with the Wireless Technology Group of Amazon Lab126, Sunnyvale, CA 94089 USA (e-mail: qh5x4@mst.edu; rrajagop@amazon.com; hosadurg@amazon.com).

Color versions of one or more figures in this article are available at https://doi.org/10.1109/TEMC.2021.3117845.

Digital Object Identifier 10.1109/TEMC.2021.3117845

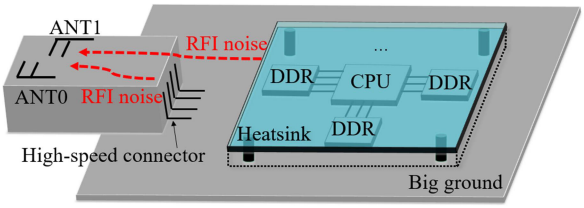


Fig. 2. Multiple noise sources in the product considered in this article.

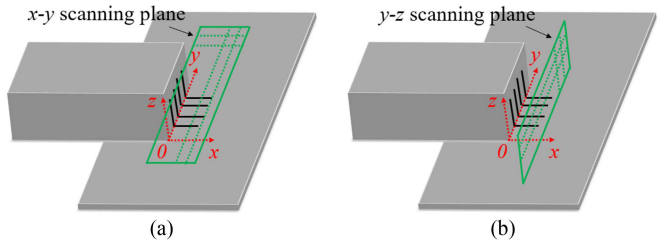


Fig. 3. (a) *x*–*y* scanning plane. (b) *y*–*z* scanning plane.

reference. However, for signals such as double-data-rate (DDR) signals [18], [19] in real products, phase measurements are more challenging because DDR signals are random binary sequences and hence can generate random broadband noise [20]. It is challenging to track a stable measured signal. Moreover, we cannot assign a synchronized signal to active DDR sources. Thus, it is difficult to find a phase reference. To analyze noise signals, such as DDR signals, some researchers have attempted to use the dipole-moment method with only the measured magnitude [20]; however, this approach works only when a single visible dipole moment is present in the near-field pattern. This method cannot handle more complicated random sources without a clear dipole-moment pattern.

In this article, a real-world product with multiple random noise sources, including various DDR memory modules and a high-speed connector, is studied. This article proposes a method of source reconstruction and RFI estimation for these sources. An approach using the VNA tuned-receiver mode is presented to resolve the phase measurement for the random DDR sources to be reconstructed with a Huygens' box. Additionally, the high-speed connector is reconstructed using an equivalent dipole. The total contribution of the Huygens' box and the equivalent dipole is further studied based on their uncorrelated relationship. The reconstructed source model is validated by comparing the simulated RFI using the source model with the measured RFI caused by the total contribution from the random noise sources.

The rest of this article is organized as follows. The source reconstruction of the high-speed connector is briefly introduced in Section II. In Section III, details are given regarding the reconstruction of the Huygens' box. In Section IV, the reconstruction of the two sources is explained. Finally, Section V concludes this article.

## II. Source Modeling for a High-Speed Connector

Fig. 2 illustrates the noise sources in the actual product considered in this article. Multiple DDR memory modules connect with a CPU located beneath a heatsink, generating RFI noise on two victim antennas. Source reconstruction for this complex scenario is challenging due to difficulties in phase measurement. Moreover, one high-speed connector is interfering with both victim antennas simultaneously, which exacerbates this problem.

The first noise source to consider is the high-speed connector, which cannot be easily addressed by the dipole-moment method, in which the near field is scanned over a plane above the device under test (DUT). The right-angle corner of the transition part is identified as the primary noise source of the connector. When measuring the connector, the heatsink was shielded entirely with gaskets to eliminate the radiation from the sources underneath. In [21], a near-field scanning method was proposed to deal with this challenging structure, and a half-dipole pattern was found through scanning. In this article, the same procedure was utilized to resolve the noise modeling for the same type of connector [21].

### A. Near-Field Scan

Near-field scanning was performed for two planes with different orientations: the *x*–*y* and *y*–*z* planes, as shown in Fig. 3. Both $H_x$ and $H_y$ were measured in these planes, with only the magnitude being measured. The spectrum analyzer (SA) settings were as follows: the measurement frequency range was 2.4–2.5 GHz, the resolution bandwidth was 100 kHz, an root mean square (RMS) detector was used, the sweep time was 117 us, 1001 samples points were measured, and a maximum hold trace mode was used. These settings were used for all of the following magnitude measurements based on an SA. In addition, all the measurements in this article were performed in a well-shielded chamber to exclude other noise signals, such as external Wi-Fi signals, from the measured noise signal.

A low-noise amplifier (LNA) was used to amplify the RFI signal by cascading three amplifiers with gain values of 10, 15, and 15 dB and noise figure values of 0.7, 3.2, and 3.2 dB, respectively. Even though the SA has a high noise figure of 24 dB, this LNA ensures a low noise figure of 1.45 dB and a high gain of 40 dB for the entire system to maximize the signal-to-noise ratio (SNR) of weak signal measurements. The same LNA was adopted for the remaining measurements throughout this article.

Similar to [21], the near-field pattern looks like half of an $M_y$ dipole, as shown in Fig. 4. The field data in Fig. 4 was obtained through a precise scanning robot with a spatial resolution of 1 mm and plotted using interpolation.

### B. Dipole Strength Extraction and RFI Simulation

In previous research [20], [22], the least-square method has been applied to extract the dipole strength of a single dipole. However, in this case, the transfer coefficient cannot be calculated analytically from the near field for a magnetic dipole in free space due to the connector structure. Thus, the strategy described in [21] is adopted in this article. Namely, a full-wave simulation was used by placing an equivalent $M_y$ dipole near the connector structure to obtain the *H* field as the transfer coefficient. More details are provided in [21].

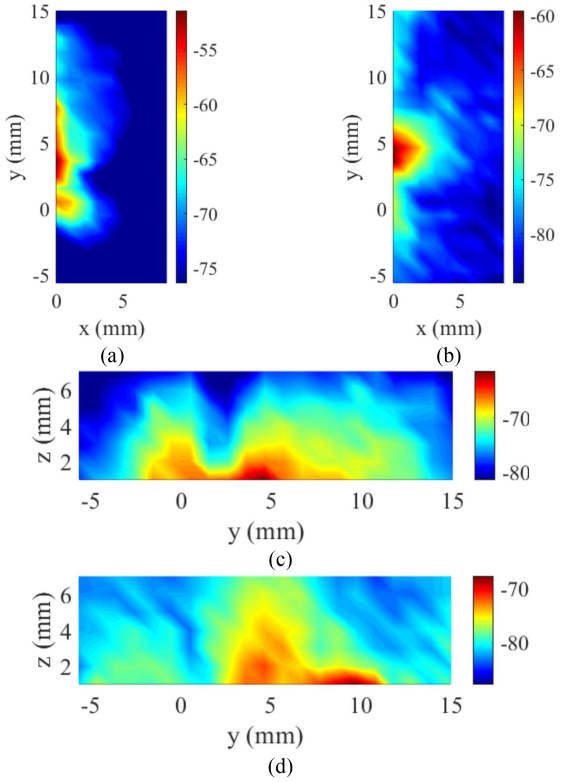


Fig. 4. Measured H field; unit: dB(A/m). (a) $H_x$ in the $x$–$y$ plane at $z = 1$ mm. (b) $H_y$ in the $x$–$y$ plane at $z = 1$ mm. (c) $H_x$ in the $y$–$z$ plane at $x = 4$ mm. (d) $H_y$ in the $y$–$z$ plane at $x = 4$ mm.

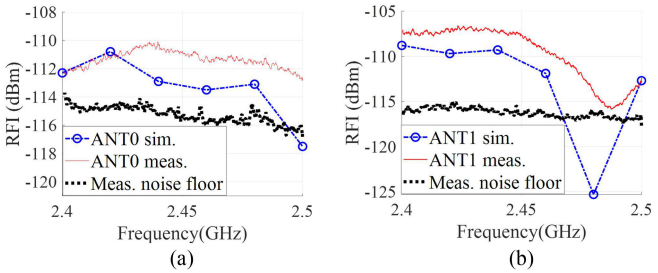


Fig. 5. Comparison of measured and simulated RFI caused by the connector. (a) ANT0. (b) ANT1.

After the dipole strength was extracted from the near field, the corresponding magnetic dipole was applied in a full-wave simulation to simulate the RFI caused by the connector. Fig. 5 compares the simulated and measured RFI for the two victim antennas. A good agreement is achieved with a discrepancy less than 4 dB, except for the resonance dip near 2.48 GHz for ANT1. This deviation is reasonable because the simulated RFI at 2.48 GHz is lower than the measurement noise floor, but the signals buried beneath the noise floor are not measurable. The measured noise signal around 2.48 GHz is the summation of thermal noise (the noise floor) and the noise signal from the connector. Therefore, the measured noise power near 2.48 GHz in Fig. 5(b) is slightly (about 1 dB) higher than the noise floor.

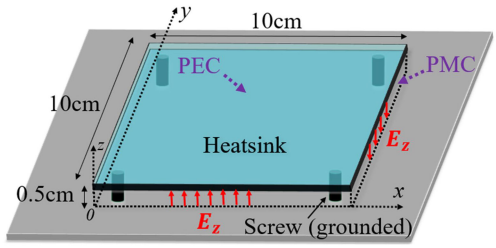


Fig. 6. Heatsink geometry information and boundary condition approximation.

## III. Source Reconstruction for DDR Sources

By utilizing the heatsink structure, a Huygens' box can be applied to reconstruct the DDR sources. In this method, the key is to measure the field phase and magnitude on the Huygens' box. Phase measurement is usually more complicated than magnitude measurement because it requires a reference. The multiple DDR sources beneath the heatsink generate random noise signals and thus make it challenging to find a stable reference signal.

This section will elaborate on approaches for measuring the field phase and magnitude from random DDR sources. When measuring the DDR sources, the radiation from the high-speed connector was eliminated by powering OFF the connector. Additionally, RFI estimation results obtained using the Huygens' box will be shown and compared with measurement results.

### A. Heatsink Structure

The detailed heatsink structure is shown in Fig. 6. The heatsink has dimensions of 10 cm × 10 cm, and there is a 5-mm-wide gap between the heatsink and the ground. There are also four screws in the four corners shorting the heatsink to the ground.

The frequency band of interest ranges from 2.4 to 2.5 GHz, corresponding to a wavelength of approximately 12 cm. The heatsink forms a cavity structure, with the top and bottom faces being PEC boundaries. The gap width is much smaller than the wavelength. Consequently, the four sides can be approximated as perfect-magnetic-conductor boundaries, as there is no significant normal current to generate a tangential H field near the four edges. Namely, only a normal $H$ field and a tangential $E$ field are present on the four sides.

According to the Huygens' equivalence principle, the normal H field does not contribute [23]; hence, only the tangential ifield is useful. The top and bottom surfaces are PEC boundaries, and consequently, the tangential E field on the top and bottom face is zero. Therefore, $E_z$ is dominant on the four sides. Thus, the problem can be resolved by measuring the magnitude and phase of $E_z$ along the gap of the four edges.

Moreover, because the gap width is sufficiently small, it can be assumed that there is nearly no field variation along the $z$-direction. In other words, only one location needs to be sampled along the z-direction, which further simplifies the measurement procedure.

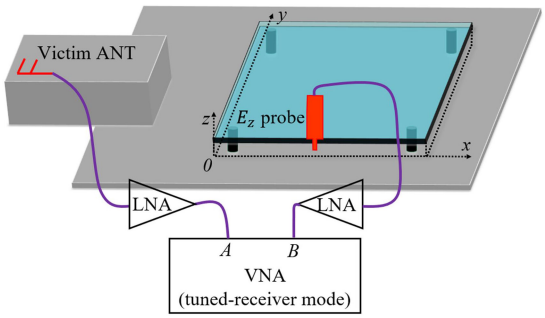


Fig. 7. Setup for measuring the phase of $E_z$ of a Huygens' box.

### B. Phase Measurement

Phase measurements require a phase reference. In most cases, a separate probe or signal line can be utilized for the phase reference. In this article, one of the victim antennas was chosen as the phase reference, as shown in Fig. 7. The victim antenna was chosen because it can receive a clear noise signal, which is needed for a good phase correlation. Using the victim antenna instead of another reference probe can avoid disturbing the movement of the $E_z$ probe, which is a broadband probe that can work up to 6 GHz [24]. Moreover, as will be explained below, the dominant source that causes the strongest noise coupling at the victim antenna can be identified by selecting the strongest peak of the reference signal.

To measure the relative phase between the victim antenna and the $E_z$ probe, an oscilloscope can be used to record their time-domain waveforms and resolve their phase difference through post-processing and fast Fourier transform [25]. However, using an oscilloscope is slow and has a low SNR [25].

Instead, the VNA tuned-receiver mode was utilized for phase measurements [25]. The tuned-receiver mode is a VNA operation mode that turns OFF the internal source and simultaneously receives signals at channels *A* and *B*. The magnitude and phase of *A* and *B* can be recorded concurrently; hence, the phase difference between the two channels can be obtained. Both *A* and *B* were amplified through an LNA to ensure detectable signals.

Fig. 8 shows the measurement results for the *A* magnitude, *B* magnitude, and phase difference between *A* and *B*, obtained by using the VNA tuned-receiver mode with a zero span at 2.437 GHz. A sweep time of 2 seconds was used, and 1601 points were obtained for each sweep. The time duration of each sweeping point is roughly 1.2 ms. The number of points on the *x*-axis in Fig. 8 represents different sweeping points, namely different time. The magnitudes of *A* and *B* were unstable and varied considerably at different sweeping points, which was expected because DDR signals are random binary sequences [20]. Unfortunately, as shown in Fig. 8(c), the phase difference between *A* and *B* also varied randomly from -180° to 180°s, not providing any helpful phase information.

The random-like variation of the measured phase difference between *A* and *B* can be understood as follows. Due to the multiple DDR noise sources distributed beneath the heatsink, channels *A* and *B* may receive signals of varying amplitudes for different sources from various locations at different moments.

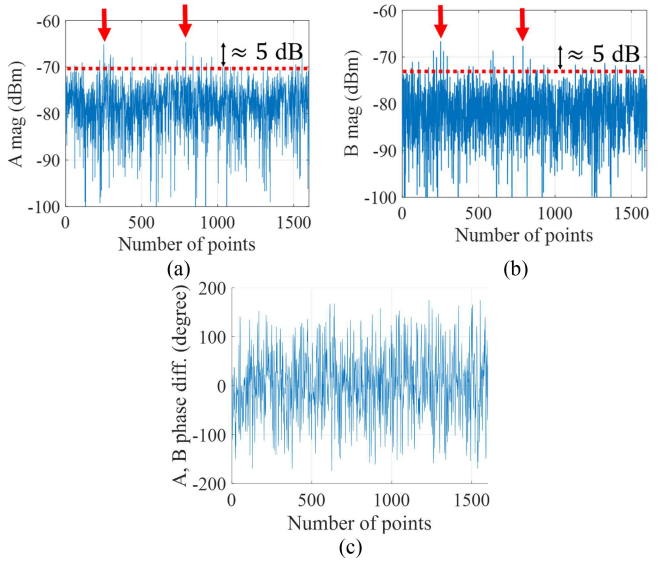


Fig. 8. Magnitudes obtained in the VNA tuned-receiver mode for a zero span at 2.437 GHz. A sweep time of 2 s was used. (a) *A* magnitude for one sweep. (b) *B* magnitude for the same sweep. (c) Phase difference between *A* and *B* for a single sweep.

Each of these sources generates random noise signals similar to those shown in Fig. 8 (a) and (b). Therefore, the phase measurement result shown in Fig. 8(c) is reasonable.

Notably, in Fig. 8 (a) and (b), when there is a peak in *A*, there is also another peak in *B*, as marked by arrows. Given this observation, it is reasonable to assume that there is one dominant source causing these peak signals. Here, $V_1$ is the dominant source; $V_2$ represents other weaker sources uncorrelated with $V_1$; $V_A$ is the coupled noise voltage for channel *A*; $V_B$ is the coupled noise voltage for channel *B*; and $k_{11}$, $k_{12}$, $k_{21}$, and $k_{22}$ represent respective transfer coefficients. The relationship between the sources and the two channels can be expressed using (1), in which all the variables are complex values with both magnitude and phase information

$$\begin{aligned} V_A &= k_{11} \cdot V_1 + k_{12} \cdot V_2 \\ V_B &= k_{21} \cdot V_1 + k_{22} \cdot V_2. \end{aligned} \tag{1}$$

If we divide both sides in (1), we can obtain

$$\frac{V_B}{V_A} = \frac{k_{21}V_1 + k_{22}V_2}{k_{11}V_1 + k_{12}V_2} = \frac{k_{21} + k_{22}\,(V_2/V_1)}{k_{11} + k_{12}\,(V_2/V_1)}. \tag{2}$$

By organizing (2), we can further obtain

$$\frac{V_B}{V_A} = \frac{k_{21}k_{11} + (k_{11}k_{22} - k_{21}k_{12})\,(V_2/V_1) - k_{22}k_{12}(V_2/V_1)^2}{k_{11}^2 - k_{12}^2(V_2/V_1)^2}. \tag{3}$$

By observing Fig. 8, we can find that the peak signals are at least 5 dB higher than the weaker signals. If we only select the peak signals as marked in Fig. 8, the signal portion from the dominant source is at least 5 dB higher than the signal portion

from the weaker sources, namely

$$20\log_{10}\left(|k_{11}V_1|/|k_{12}V_2|\right) > 5 \text{ dB}. \tag{4}$$

Therefore, we can easily obtain

$$20\log_{10}\left(|k_{12}V_2|^2 \Big/ |k_{11}V_1|^2\right) < -10 \text{ dB} \tag{5}$$

where -10 dB is considered as a small value that can be neglected in engineering practice. Thus, it is reasonable to conclude

$$|k_{12}V_2|^2 \ll |k_{11}V_1|^2 \tag{6}$$

which is equivalent to

$$k_{12}^2(V_2/V_1)^2 \ll k_{11}^2. \tag{7}$$

Therefore, the quadratic term $k_{12}^2(V_2/V_1)^2$ in the denominator of (3) can be neglected.

Similarly, the peak signals in channel *B* correlated with the peak signals in channel *A* were also be selected, so that (8) is satisfied

$$k_{22}^2(V_2/V_1)^2 \ll k_{21}^2. \tag{8}$$

Through (7) and (8), we can obtain

$$k_{22}k_{12}(V_2/V_1)^2 \ll k_{21}k_{11}. \tag{9}$$

Consequently, the quadratic term $k_{22}k_{12}(V_2/V_1)^2$ in the numerator of (3) can also be neglected. Hence, (3) can be approximated as

$$\frac{V_B}{V_A} \approx \frac{k_{21}}{k_{11}} + \frac{k_{11}k_{22} - k_{21}k_{12}}{k_{11}^2} \cdot \frac{V_2}{V_1}. \tag{10}$$

We can take an average on both sides of (10) and obtain

$$\left\langle \frac{V_B}{V_A} \right\rangle = \frac{k_{21}}{k_{11}} + \frac{k_{11}k_{22} - k_{21}k_{12}}{k_{11}^2} \cdot \left\langle \frac{V_2}{V_1} \right\rangle. \tag{11}$$

According to [27], if $V_1$ and $V_2$ are two random variables with normal distributions and zero means (which is valid for the random signals in this article), the second term in (11) is approximately equal to 0. Namely, the phase difference between $V_B$ and $V_A$ caused by the dominant source can be resolved [27] by using

$$\left\langle \frac{V_B}{V_A} \right\rangle \approx \frac{k_{21}}{k_{11}}. \tag{12}$$

Based on the above analysis, the peak signals must be selected to acquire meaningful phase information. Thus, the procedure shown in Fig. 9 was adopted to measure the phase difference between *B* and *A*. First, one sweep was performed in the VNA tuned-receiver mode using a zero span for 2 s, and all channels were held. Second, the highest peak in the *A* magnitude was selected, and the *A* phase, *B* magnitude, and *B* phase at the same point were read. Third, multiple sweeps were performed, and the corresponding values for each sweep were recorded by repeating the second step. Finally, the average value of *B*/*A* for multiple sweeps was calculated to obtain the phase difference between *B* and *A*.

Following the above procedure, the phase at $y = 0$ cm, $x = 5$ cm was measured by performing 40 sweeps at 2.437 GHz. In addition, the device was power-cycled, and a second measurement

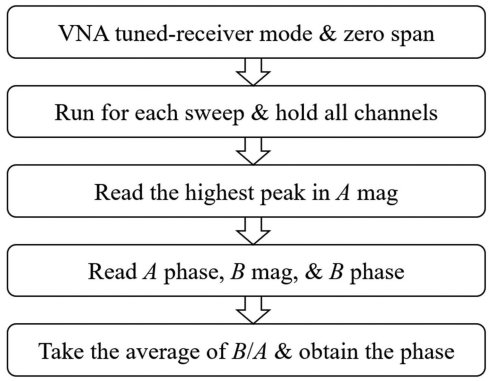


Fig. 9. Procedure for measuring the phase difference between *B* and *A*.

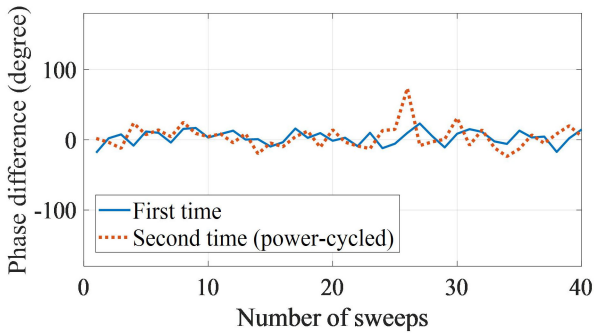


Fig. 10. Measured phase at $y = 0$ cm, $x = 5$ cm after the highest peak in the *A* magnitude was chosen for each sweep; the first and second cycles (when the device was power-cycled) show good agreement. The sweep time was 2 s, and the intermediate frequency bandwidth was 5 kHz.

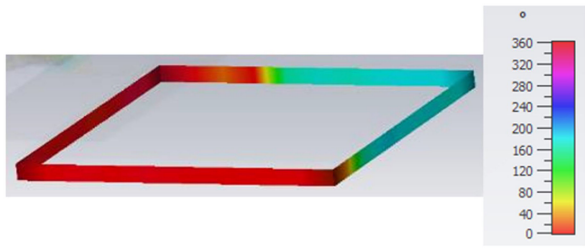


Fig. 11. Measured phase distribution at 2.437 GHz (unit: degrees). The interval between two adjacent measurement points is 1 cm.

was performed. The phase results of the two measurements are plotted in Fig. 10, showing a phase difference near 0 degrees. The standard deviations for the two curves in Fig. 10 are 16.8° and 9.9°, respectively. Despite slight fluctuations, the measured phase is more consistent than that shown in Fig. 8(c), which supports the initial assumption that one dominant source is causing the correlated peak signals in channels *A* and *B*.

Using the same procedure, the phase values at other locations were measured, and the phase distribution at 2.437 GHz is shown in Fig. 11. Furthermore, by measuring the phase at different frequencies, we found that the phase distribution changed little with frequency. Fig. 12 (a) and (b) presents the phase measured at different frequencies for two distinct locations. The results

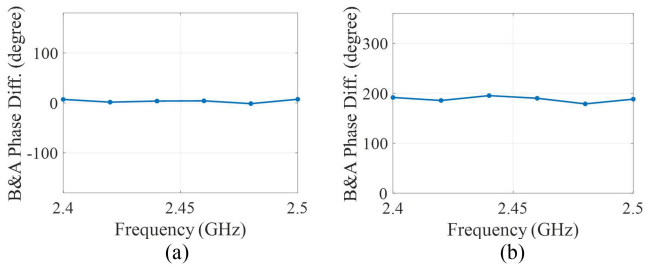


Fig. 12. (a) Phases for different frequencies at $x = 4$ cm, $y = 0$ cm, which are all near 0°. (b) Phases for different frequencies at $x = 8$ cm, $y = 10$ cm, which are all near 180°.

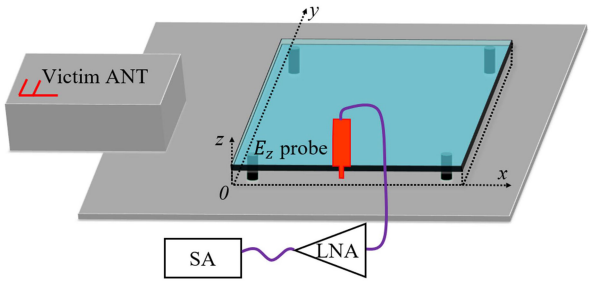


Fig. 13. Setup for measuring the magnitude of $\boldsymbol{E_z}$ for the Huygens' box.

indicate that the dominant sources for different frequencies may be located at the same place.

### C. Magnitude Measurement

Because most of the available VNAs have poor image rejection in the tuned-receiver mode, they cannot perform as well as an SA receiver [25]. In the VNA tuned-receiver mode, an unwanted image signal arises, comparable in magnitude to the wanted signal. Some researchers use a zero span to avoid the unwanted image signal when using VNA to measure single-frequency signals [25]. However, the noise signal in this article is broadband. Thus, the magnitude of different frequencies cannot be separated when using the VNA tuned-receiver mode. Consequently, to obtain accurate magnitude measurements, an SA with better image rejection was used to measure the $E_z$ magnitude on the Huygens' box, based on the setup shown in Fig. 13.

Because the assumption of a single dominant source has been validated, it is reasonable to use a maximum hold trace mode in the SA to measure the maximum $E_z$ magnitude generated by the assumed dominant source. The SA settings described for the connector measurement in Section II were utilized in this case. Fig. 14 presents two examples of the measured magnitude distribution at two different frequencies.

### D. RFI Simulation for a Huygens' Box

The phase and magnitude at different frequencies were measured by VNA and an SA, respectively. A separate Huygens' box model with the measured $E_z$ magnitude and phase was employed for each frequency point. These Huygens' box models

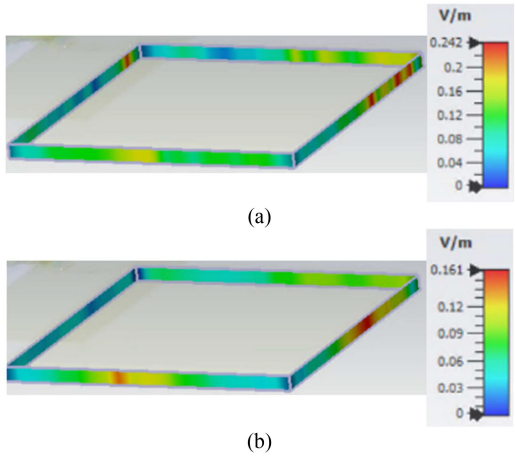


Fig. 14. Two examples of the measured magnitude distribution. The interval between measurement points was 1 cm. (a) At 2.40 GHz. (b) At 2.48 GHz.

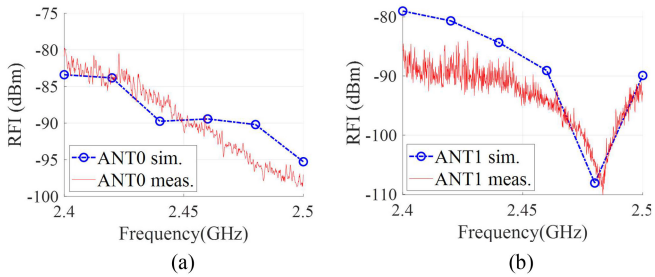


Fig. 15. Comparison between the simulated and measured RFI for the Huygens' box. (a) ANT0. (b) ANT1.

were imported into the ∗CST Studio Suite [26] to simulate the RFI at different frequencies. Additionally, the RFI values in the actual product were measured by an SA using the same settings utilized for the $E_z$ magnitude.

The simulated and measured RFI results for both victim antennas are compared in Fig. 15. The maximum deviation is approximately 5 dB. This good agreement indicates that the preassumption of one dominant source is reasonable, and the proposed method of phase and magnitude measurement for reconstructing multiple DDR sources is effective.

## IV. Multiple Noise Source Quantification

Although the DDR memory noise dominates the RFI in the particular DUT studied in the previous sections, it is also common for multiple noise sources to have comparable contributions to the RFI. Noise source quantification for such a case is investigated in this section. To ensure that the contribution from each noise source is comparable, the DDR source was set to operate in a different mode to reduce the noise strength. In addition, three sides of the heatsink gap were shielded with gaskets to reduce the coupling to the victim antennas. The structure of the so-called "one-side" heatsink is depicted in Fig. 16. To reconstruct the noise source for this structure, measurements are needed only for the unshielded side.

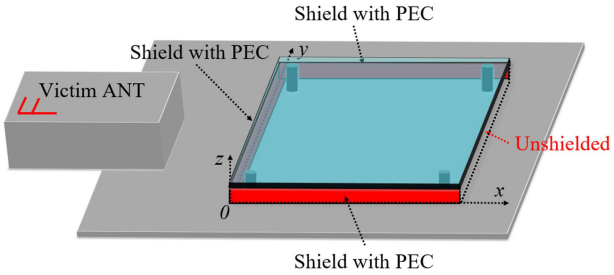


Fig. 16. Structure of the "one-side" heatsink. Three sides of the heatsink are shielded in another operation mode with lower emission.

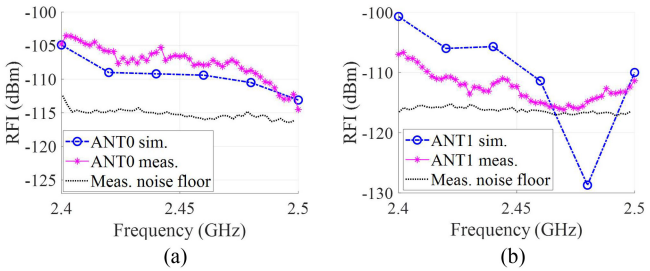


Fig. 17. Comparison of measured and simulated RFI for the "one-side" heatsink. (a) ANT0. (b) ANT1.

### A. Heatsink Source Reconstruction

By applying the procedure described in Section III, the magnitude and phase of $E_z$ were measured along the open side of the heatsink. Using these measurements, the Huygens' box models at different frequencies were again imported into the CST Studio Suite [26] to simulate the RFI. Similar to Fig. 15, the RFI predicted by the Huygens' box models for the "one-side" heatsink is reasonably close to the measured RFI, within an error of 5 dB, as shown in Fig. 17. This good agreement provides a second verification of our proposed method for reliably and accurately reconstructing DDR sources.

### B. Reconstruction of Two Noise Sources

In the DUT, the two noise sources come from two different unsynchronized functioning modules. Thus, these two sources are expected to have uncorrelated radiation. We performed two more measurements to confirm their uncorrelated relationship. First, we used an SA to measure their frequency spectrum and observed two distinct time-varying spectrum characteristics. Second, we used a VNA with tuned-receiver mode to measure the phase difference between their radiation field and could not observe any phase correlation. We can do the following mathematical derivations to analyze the total noise power received by an SA from these two uncorrelated sources.

Suppose that $X_1$ and $X_2$ are two signals with a phase difference of $\theta$, namely

$$\frac{X_1}{X_2} = \frac{|X_1|}{|X_2|} \cdot e^{j\theta}. \tag{13}$$

If $X_1$ and $X_2$ are correlated with each other, their phase difference $\theta$ is a constant value. However, since the heatsink and the connector have been identified as uncorrelated, their phase difference $\theta$ is a random value between 0 and 360 degrees at different times.

When using an RMS detector, which is commonly used for RFI measurements of noise-like signals, the SA calculates and outputs the average power of all samples for each measurement point. Thus, using an RMS detector has an averaging effect that can benefit the repeatability of power measurement for complex and random signals. Suppose that $X(i)$ represents the voltage of the $i$th sample on a measurement point, and $N$ is the total number of samples belonging to this point. Using the RMS detector, the displayed power value for this point can be expressed as

$$P_{\mathrm{RMS}} = \left(\sum_{i=1}^{N} |X(i)|^2\right) \Big/ N. \tag{14}$$

Hence, using the RMS detector, the total power from $X_1$ and $X_2$ is calculated as

$$P_{\mathrm{RMS}} = \left(\sum_{i=1}^{N} \left||X_1(i)| + |X_2(i)| \cdot e^{j\theta(i)}\right|^2\right) \Big/ N. \tag{15}$$

By rearranging (15), the total power can be derived as

$$P_{\mathrm{RMS}} = \left(\sum_{i=1}^{N} |X_1(i)|^2\right) \Big/ N + \left(\sum_{i=1}^{N} |X_2(i)|^2\right) \Big/ N + \left(\sum_{i=1}^{N} 2\,|X_1(i)| \cdot |X_2(i)| \cdot \cos[\theta(i)]\right) \Big/ N. \tag{16}$$

If $X_1$ and $X_2$ are uncorrelated, their phase difference $\theta$ is a random number. Thus, the value of $\cos[\theta(i)]$ is randomly distributed between -1 and 1. If $N$ is large, the third term in (16) will be approximately equal to 0, as shown

$$\left(\sum_{i=1}^{N} 2\,|X_1(i)| \cdot |X_2(i)| \cdot \cos[\theta(i)]\right) \Big/ N \approx 0. \tag{17}$$

Therefore, the total power from the two uncorrelated signals obtained by the RMS detector is approximately equal to

$$P_{\mathrm{tot}} \approx \left(\sum_{i=1}^{N} |X_1(i)|^2\right) \Big/ N + \left(\sum_{i=1}^{N} |X_2(i)|^2\right) \Big/ N. \tag{18}$$

The result (18) is simply the power summation of $X_1$ and $X_2$ obtained by the RMS detector. This derivation outcome shows that the total noise power is expected to be the summation of the noise power components from the two uncorrelated sources determined by the RMS detector.

Thus, the RFI noise was measured from these two sources to validate the above expectation. The RFI measured from the "one-side" heatsink is shown in Fig. 17, which is comparable to the RFI measured from the connector. In the RFI measurement using an SA, the settings listed in Section II were used.

The RFI level for the two sources with simultaneous contributions is plotted in Fig. 18. The "connector + one-side heatsink' curves mean the measured RFI power values when the two sources were working simultaneously; the "power sum" curves

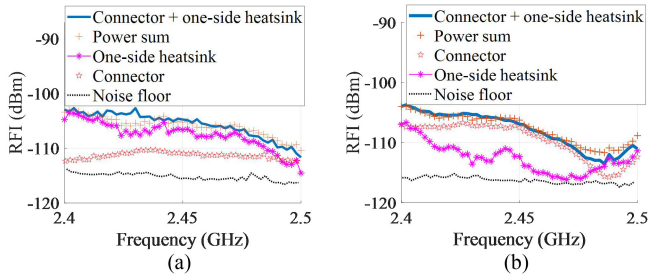


Fig. 18. RFI comparison when the two sources are coexisting. (a) ANT0. (b) ANT1.

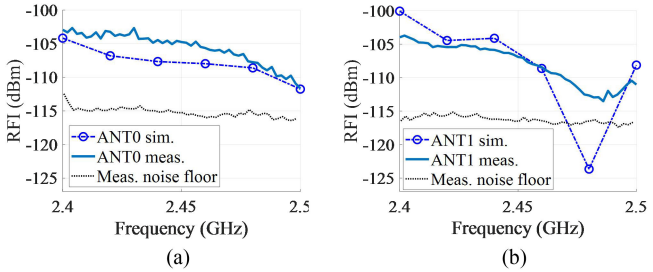


Fig. 19. Comparison of measured and simulated RFI for the connector plus the "one-side" heatsink. (a) ANT0. (b) ANT1.

represented the mathematical summation of the power values from the two sources when they were radiating individually. As shown in Fig. 18, the total noise power from the two noise sources, which corresponds to the worst case, agrees with the noise power summation from these two respective sources. This finding corroborates their uncorrelated relation and the conclusions derived from the above mathematical analysis.

Finally, in simulation, the two RFI sources, including the "one-side" heatsink and the connector, were combined to predict the total RFI by summing the noise powers of the two separate simulations. The simulated RFI matches well with the measured RFI from the two coexisting sources, with a discrepancy of less than 5 dB, as shown in Fig. 19.

## V. Conclusion

A novel approach for reconstructing multiple random noise sources in a real product is presented. The noise sources include random DDR sources and a high-speed connector. Using the VNA tuned-receiver mode and assuming one dominant source, we can obtain the field phase induced by the random DDR sources and subsequently reconstruct a Huygens' box. By extracting the dominant source phase, we resolved the challenge in measuring the phase of multiple DDR noise sources. Additionally, mathematical derivations show that the total RFI from two uncorrelated noise sources can be obtained by summing the respective noise power from each source using an RMS detector, and this finding was validated through measurements. Eventually, the simulated RFI using the reconstructed model agrees with the measured RFI from these random noise sources with a deviation less than 5 dB.

This article proposes two strategies for reconstructing the multiple random noise sources. The first strategy is to retrieve the phase from multiple random sources by assuming one dominant source, which was used for reconstructing the DDR sources beneath the heatsink. Nevertheless, the type of random sources is not limited to DDR signals for the proposed methodology. The concept can be extended to other random signals for which it is difficult to track a stable reference signal for phase measurement. The second strategy is to consider the worst-case coupling for two uncorrelated sources by summing up their power values using the RMS detector.

In summary, this article demonstrates a source reconstruction solution for complex random noise signals by focusing on the dominant source and the worst-case noise coupling among multiple random sources.

## References

[1] Z. Yu, J. A. Mix, S. Sajuyigbe, K. P. Slattery, and J. Fan, "An improved dipole-moment model based on near-field scanning for characterizing near-field coupling and far-field radiation from an IC," *IEEE Trans. Electromagn. Compat.*, vol. 55, no. 1, pp. 97–108, Feb. 2013.

[2] H. H. Park, H. B. Park, and H. S. Lee, "A simple method of estimating the radiated emission from a cable attached to a mobile device," *IEEE Trans. Electromagn. Compat.*, vol. 55, no. 2, pp. 257–264, Apr. 2013.

[3] H. H. Park, H. T. Jang, H. B. Park, and C. Choi, "An EMI evaluation method for integrated circuits in mobile devices," *IEEE Trans. Electromagn. Compat.*, vol. 55, no. 4, pp. 780–787, Aug. 2013.

[4] S. Shinde *et al.*, "Investigating intra-system radio-frequency interference from high-speed traces to a GPS patch antenna," in *Proc. Int. Symp. IEEE Electromagn. Compat* ., 2013, pp. 7–11.

[5] S. Shinde *et al.*, "Investigation of interference in a mobile phone from a DC-to-DC converter," in *Proc. Int. Symp. IEEE Electromagn. Compat.*, 2013, pp. 616–620.

[6] G. Shen, S. Yang, J. Sun, S. Xu, D. J. Pommerenke, and V. V. Khilkevich, "Maximum radiated emissions evaluation for the heatsink/IC structure using the measured near electrical field," *IEEE Trans. Electromagn. Compat.*, vol. 59, no. 5, pp. 1408–1414, Oct. 2017.

[7] Q. Huang *et al.*, "Reciprocity theorem based RFI estimation for heatsink emission," in *Proc. Int. Symp. IEEE Electromagn. Compat.*, 2019, pp. 590–594.

[8] Q. Huang *et al.*, "A novel RFI mitigation method using source rotation," *IEEE Electromagn. Compat.*, vol. 63, no. 1, pp. 11–18, Feb. 2021.

[9] X. Tong, "Simplified equivalent modelling of electromagnetic emissions from printed circuit boards," Ph.D. dissertation, Univ. Nottingham, Nottingham, U. K., 2010.

[10] P. F. Lopez, C. Arcambal, D. Baudry, S. Verdeyme, and B. Mazari, "Simple electromagnetic modeling procedure: From near-field measurements to commercial electromagnetic simulation tool," *IEEE Trans. Instrum. Meas.*, vol. 59, no. 12, pp. 3111–3121, Dec. 2010.

[11] J. Pan *et al.*, "Application of dipole-moment model in EMI estimation," in *Proc. IEEE Int. Symp. Electromagn. Compat*., 2015, pp. 350–354.

[12] J. Pan *et al.*, "Radio-Frequency interference estimation using equivalent dipole-moment models and decomposition method based on reciprocity," *IEEE Trans. Electromagn. Compat.*, vol. 58, no. 1, pp. 75–84, Feb. 2016.

[13] C. Wu *et al.*, "Estimating the near field coupling from SMPS circuits to a nearby antenna using dipole moments," in *Proc. Int. Symp. IEEE Electromagn. Compat* ., 2016, pp. 353–357.

[14] Q. Huang and J. Fan, "Machine learning based source reconstruction for RF desense," *IEEE Trans. Electromagn. Compat.*, vol. 60, no. 6, pp. 1640–1647, Dec. 2018.

[15] H. Wang, V. Khilkevich, Y. Zhang, and J. Fan, "Estimating radio-frequency interference to an antenna due to near-field coupling using decomposition method based on reciprocity," *IEEE Trans. Electromagn. Compat.*, vol. 55, no. 6, pp. 1125–1131, Dec. 2013.

[16] L. Li *et al.*, "Radio-frequency interference estimation by reciprocity theorem with noise source characterized by Huygens's equivalent model," in *Proc. Int. Symp. IEEE Electromagn. Compat* ., 2016, pp. 358–363.

[17] M. Sørensen, I. B. Bonev, O. Franek, and G. F. Pedersen, "Assessment of the Huygens' box method with different sources near obstacles," *IEEE Trans. Electromagn. Compat.*, vol. 62, no. 2, pp. 433–442, Apr. 2020.

[18] D. Han, H. Hsu, J. Chen, M. Schaffer, C. M. Cheung, and P. Davuluri, "PC client platform RFI risks and mitigation methodologies," in *Proc. Int. Symp. IEEE Electromagn. Compat* ., 2015, pp. 85–90.

[19] Y. Ho, H. Hsu, and J. Lee, "Optimal decoupling strategy to suppress radio frequency interference (RFI) from double data-rate (DDR) memory power-plane radiation," in *Proc. Int. Symp. IEEE Electromagn. Compat.*, 2017, pp. 537–542.
[20] Q. Huang *et al.*, "Desense prediction and mitigation from DDR noise source," in *Proc. Int. Symp. IEEE Electromagn. Compat.*, 2018, pp. 139–144.
[21] L. Zhang *et al.*, "Accurate RFI prediction of 3D Non-planar connector with half magnetic dipole pattern," in *Proc. IEEE Joint Int. Symp. Electromagn. Compat., Sapporo Asia-Pacific Int. Symp. Electromagn. Compat.*, 2019, pp. 770–773.
[22] Q. Huang *et al.*, "Physics-Based dipole moment source reconstruction for RFI on a practical cellphone," *IEEE Trans. Electromagn. Compat.*, vol. 59, no. 6, pp. 1693–1700, Dec. 2017.
[23] C. Balanis, *Advanced Engineering Electromagnetics*. New York, NY, USA: Wiley, 1999.
[24] G. Li, K. Itou, Y. Katou, N. Mukai, D. Pommerenke, and J. Fan, "A resonant E-Field probe for RFI measurements," *IEEE Trans. Electromagn. Compat.*, vol. 56, no. 6, pp. 1719–1722, Dec. 2014.
[25] S. Marathe *et al.*, "Spectrum analyzer-based phase measurement for near-field EMI scanning," *IEEE Trans. Electromagn. Compat.*, vol. 62, no. 3, pp. 848–858, Jun. 2020.
[26] CST Studio Suite, 2019. [Online]. Available: https://www.cst.com.
[27] T. Li *et al.*, "Phase-resolved near-field scan over random fields." *IEEE Trans. Electromagn. Compat.*, vol. 58, no. 2, pp. 506–511, Apr. 2016.

**Ling Zhang** (Student Member, IEEE) received the B.S. degree in electrical engineering from the Huazhong University of Science and Technology, Wuhan, China, in 2015, and the M.S. and Ph.D. degrees in electrical engineering from Missouri University of Science and Technology, Rolla, MO, USA, in 2017 and 2021 respectively.

From August 2016 to August 2017, he was a Student Intern with Cisco. He was a Post-doctoral Researcher with Zhejiang University, Hangzhou, China. His research interests include machine learning, electromagnetic interference, signal integrity, power integrity, and radio-frequency interference.

**Haochen Yang** (Student Member, IEEE) received the B.E. degree in microelectronic science and engineering in 2020 from Zhejiang University, Hangzhou, China, where he is currently working toward the Ph.D. degree in electrical engineering with the College of Information Science and Electronic Engineering.

In the summer of 2019, he was an Intern with the EMC Laboratory, Missouri S&T, Rolla, MO, USA.

**Xiangrui Su** (Student Member, IEEE) received the B.S. degree in electrical engineering from Zhejiang University, Hangzhou, China, in June 2019. Since 2019, he has been working toward the Ph.D. degree in electrical engineering with the Electromagnetic Compatibility Laboratory of the Missouri University of Science and Technology, Rolla, MO, USA.

He was a Student Intern with Apple, Cupertino, CA, USA. His research interests include RFI source reconstruction and coupling paths analysis, and the conductive emission modeling based on hybrid simulation.

**Qiaolei Huang** received the B.E. degree in electrical and computer engineering from the Huazhong University of Science and Technology, Wuhan, China, in 2013, and the M.S. and Ph.D. degrees in electrical engineering from Missouri S&T, Rolla, MO, USA, in 2016 and 2019, respectively.

He was with the EMC Laboratory, Missouri S&T. His research interests include RFI, radiated emission modeling, and EMC measurement methods.

Dr. Huang was the recipient of the best papers of DesignCon 2018, DesignCon 2019, and the 2018 Joint IEEE EMC and APEMC Symposium.

**Jagan Rajagopalan** received the master's degree in wireless technology from the University of South Florida, Tampa, FL, USA, in 2010.

He is currently a Senior RF System Engineer and an Engineering Leader with the Wireless Technology Group, Amazon Lab126, Sunnyvale, CA, USA. He has more than ten years of work experience in the consumer electronics industry. He is the author of multiple IEEE conference papers and holds multiple U.S. patents in the fields of defense, EMI, and RF system design.

**Deepak Pai** received the master's degree in electrical engineering from the University of Texas at Dallas, Richardson, TX, USA, in 2014.

He is a Wireless Systems Engineer and an RF System/EM Engineer with the Wireless Technology Group, Amazon Lab126, Sunnyvale, CA, USA. He has five years of work experience in the consumer electronics industry. He is the author of multiple IEEE conference papers and holds multiple U.S. Patents in the fields of EM and antenna design.

**Chulsoon Hwang** (Senior Member, IEEE) received the B.S., M.S., and Ph.D. degrees in electrical engineering from the Korea Advanced Institute of Science and Technology, Daejeon, South Korea, in 2007, 2009, and 2012, respectively.

He was with Samsung Electronics, Suwon, South Korea, as a Senior Engineer, from 2012 to 2015. In July 2015, he was with the Missouri University of Science and Technology (formerly University of Missouri-Rolla), Rolla, MO, USA, where he is currently an Assistant Professor. His research interests include RF desense, signal/power integrity in high-speed digital systems, EMI/EMC, hardware security, and machine learning.

Dr. Hwang was a recipient of the AP-EMC Young Scientist Award, the Google Faculty Research Award, and Missouri S&T's Faculty Research Award. He was a co-recipient of the IEEE EMC Best Paper Award, the AP-EMC Best Paper Award, and a two-time co-recipient of the DesignCon Best Paper Award.

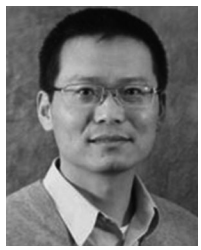

**Jun Fan** (Fellow, IEEE) received B.S. and M.S. degrees from Tsinghua University, Beijing, China, and the Ph.D. from Missouri S&T, Rolla, MO, USA, in 1994, 1997, and 2000, respectively, all in electrical engineering.

From 2000 to 2007, he was a Consultant Engineer with NCR Corporation, San Diego, CA, USA. In July 2007, he was with Missouri S&T, where he was a Professor and the Director of the EMC laboratory. He was the Director of the National Science Foundation Industry/University Cooperative Research Center for Electromagnetic Compatibility and as a Senior Investigator with the Missouri S&T Material Research Center. He is currently an Adjunct Professor with Missouri S&T. His research interests include signal integrity and EMI design in high-speed digital systems, dc power-bus modeling, intrasystem EMI and RFI, PCB noise reduction, differential signaling, and cable/connector designs.

Dr. Fan was the recipient of the IEEE EMC Society Technical Achievement Award in August 2009. He is currently an Associate Editor for the IEEE TRANSACTIONS ON ELECTROMAGNETIC COMPATIBILITY and IEEE EMC MAGAZINE.